Nanoscale Horizons

ROYAL SOCIETY OF CHEMISTRY

COMMUNICATION

View Article Online
View Journal | View Issue

Cite this: *Nanoscale Horiz.*, 2026, 11, 498

Received 15th August 2025,
Accepted 6th November 2025

DOI: 10.1039/d5nh00584a

rsc.li/nanoscale-horizons

Topochemical synthesis of mesoporous TiO_2 co-doped with nitrogen and fluorine for improved photocatalytic O_2 evolution under visible light

Shuwei Liu, [a] Ryosuke Nishikubo, [bc] Fumitaka Ishiwari, [bc] Xian Zhang, [a] Megumi Okazaki, [a] Shunsuke Nozawa, [d] Akinori Saeki [bc] and Kazuhiko Maeda *[ae]

Mesoporous rutile TiO_2 photocatalysts co-doped with N and F were synthesized *via* a topotactic ammonolysis approach using mesostructured TiO_2 as a precursor. The co-substitution of N and F into the rutile lattice led to substantial modulation of the Ti electronic structure and to extension of visible-light absorption, accompanied by local distortion of TiO_6 octahedra. Systematic characterization revealed that the balance between dopant incorporation and structural integrity of the mesoporous framework played a decisive role in determining photocatalytic performance for half-cell O_2 evolution. Although higher-temperature ammonolysis promoted N incorporation and enhanced visible-light absorption, it also compromised the mesostructure, reducing the overall activity. The highest O_2 evolution rate under visible-light irradiation was achieved with the sample prepared under optimal conditions that maintained both phase-pure rutile and mesoporosity. These results highlight the importance of controlling both chemical doping and structural features when designing high-performance non-metal-doped oxide photocatalysts for solar-driven water oxidation.

New concepts

We report a topotactic ammonolysis strategy to synthesize mesoporous rutile TiO_2 co-doped with nitrogen and fluorine, achieving simultaneous control over crystal phase, lattice electronic structure, and mesostructural integrity. While non-metal doping of TiO_2 has long been explored to extend visible-light activity, the challenge of preserving a high-surface-area mesoporous framework during high-temperature treatments remains largely unsolved. Our approach uniquely balances lattice substitution with mesoporous preservation, enabling co-modulation of band-gap and defect chemistry without sacrificing the hierarchical pore network essential for mass transport. This synergy allows efficient separation and transfer of photogenerated charge carriers, yielding significantly enhanced visible-light-driven O_2 evolution. The work provides a conceptual advance by demonstrating that photocatalytic performance in doped oxides is not dictated solely by light-harvesting ability, but by a fine interplay between electronic tuning and nanostructural stability. This insight is broadly applicable to the design of next-generation non-metal-doped oxides for solar energy conversion, electrocatalysis, and environmental remediation, where multifunctional structural control at the nanoscale is required.

Introduction

Photocatalytic water splitting is a promising strategy for converting abundant solar energy into clean H_2 fuel in an environmentally friendly manner.[1–4] Among the two half-reactions, water oxidation remains a major challenge because of its complex four-electron transfer process, which often limits the overall efficiency of the system.[5,6] To overcome this bottleneck, researchers have directed extensive efforts toward developing visible-light-responsive photocatalysts with enhanced charge separation and surface reactivity.[1]

Mixed-anion compounds such as oxysulfides, oxyhalides, and oxynitrides have attracted attention because of their unique electronic structures and properties originating from the incorporation of additional anionic species.[7–11] Among these compounds, oxynitrides have emerged as promising photocatalysts capable of absorbing visible light, primarily because of the contribution of N 2p orbitals to the valence band. However, N doping in oxides such as TiO_2 can induce O vacancies, which accelerate charge recombination.[12] To address this problem, researchers have proposed co-doping with F (*via* the substitution $2O^{2-} \rightleftharpoons N^{3-} + F^{-}$) to suppress recombination by balancing the local charge and maintaining

[a] *Department of Chemistry, School of Science, Institute of Science Tokyo, 2-12-1-NE-2 Ookayama, Meguro-ku, Tokyo 152-8550, Japan. E-mail: maeda@chem.sci.isct.ac.jp*
[b] *Department of Applied Chemistry, Graduate School of Engineering, Osaka University, 2-1 Yamadaoka, Suita, Osaka 565-0871, Japan*
[c] *Innovative Catalysis Science Division, Institute for Open and Transdisciplinary Research Initiatives (ICS-OTRI), Osaka University, 1-1 Yamadaoka, Suita, Osaka 565-0871, Japan*
[d] *Institute of Materials Structure Science, High Energy Accelerator Research Organization, 1-1 Oho, Tsukuba, Ibaraki 305-0801, Japan*
[e] *Research Center for Autonomous Systems Materialogy (ASMat), Institute of Science Tokyo, 4259 Nagatsuta-cho, Midori-ku, Yokohama, Kanagawa 226-8501, Japan*

the anion framework.[13–15] Indeed, N,F-co-doped TiO_2 has shown enhanced activity toward photocatalytic water oxidation.[14,16]

Mesoporous materials often exhibit improved photocatalytic performance because of their short charge carrier diffusion lengths and high surface areas, which facilitate surface chemical reactions.[17,18] For example, mesoporous TiO_2 has been reported to effectively photocatalyze the decomposition of organic dye molecules such as rhodamine B and methylene blue, as well the photoreduction of CO_2 to methane.[19–21] Mesoporous TiO_2 was first synthesized *via* a modified sol–gel method in the presence of phosphate surfactants by Antonelli and Ying in 1995.[22] Since then, considerable efforts have been devoted to developing mesoporous-structured TiO_2. Such materials are particularly interesting because of their ability to interact with atoms, ions, molecules, and nanoparticles not only on the surface but also throughout the bulk.[23] Nevertheless, developing a new template-free route to synthesize highly organized mesoporous TiO_2 spheres remains challenging because of the limited availability of appropriate precursors, poor controllability of the reactivity of transition-metal precursors, and structural collapse during crystallization and during grain growth upon heat treatment.[24,25]

This study combines two effective strategies for designing efficient water oxidation photocatalysts: (1) the formation of active, crystalline mesoporous TiO_2 *via* a microwave-assisted, template-free solvothermal method and (2) bandgap narrowing through N and F co-substitution. Although N,F-co-doped mesoporous TiO_2 (meso-TiO_2:N,F) has been widely investigated for use in applications such as the photodegradation of organic substances, its application in visible-light-driven water oxidation has not yet been reported. To the best of our knowledge, this work is the first demonstration of such a material being applied to photocatalytic water oxidation under visible light.

In the present work, meso-TiO_2:N,F is synthesized by a topochemical reaction—a powerful approach previously shown to be effective for obtaining various mixed-anion phases.[26–29] However, the potential of topochemical methods for synthesizing mesoporous mixed-anion materials has not yet been sufficiently elucidated, nor have their photocatalytic properties. In particular, this study focuses on clarifying the correlation between the mesoporous structure and the O_2 evolution rate from aqueous $AgNO_3$ by systematically comparing meso-TiO_2, meso-TiO_2:N, and meso-TiO_2:N,F. Our results demonstrate that moderate N doping both preserves the mesoporous structure and promotes photocatalytic water oxidation under visible light.

Experimental

Materials and reagents

Rutile TiO_2 (Catalysis Society of Japan Reference Catalyst, JRC-TIO-6), rutile TiO_2 (Wako Pure Chemicals, 99.0%), titanium(IV) tetrabutoxide (TBOT, Wako Pure Chemicals, 95.0%), hexane (Wako Guaranteed Reagent, >96.0%), $(NH_4)_2TiF_6$ (Wako Pure Chemicals, 95.0%), $AgNO_3$ (Wako Pure Chemicals, 99.8%), La_2O_3 (TCI, 99.9%), HCl (Kanto Chemicals, 35–37%), ethanol (Wako Guaranteed Reagent, >99.5%), acetone (Wako 1st Grade, >99.0%) were used as received.

Synthesis of meso-TiO_2

TBOT (2.5 mL) was added to a mixture of hexane (25 mL) and HCl (2.5 mL) in a pressure-tight vessel, and the mixture was heated at 423 K for 4 h using a Mars 6 microwave reaction system (CEM Japan). The resultant precipitate was collected by filtration, washed several times with ethanol and distilled water, and then dried in an oven at 353 K.

An agate mortar and pestle were used to mix the as-prepared TiO_2 with $(NH_4)_2TiF_6$ in different molar ratios in the presence of acetone. For convenience, the molar concentration of $(NH_4)_2TiF_6$ in the mixture is denoted as C (mol%), calculated using the equation

$$C = \frac{\text{Moles of } (NH_4)_2TiF_6}{(\text{moles of } TiO_2) + (\text{moles of } (NH_4)_2TiF_6)} \times 100(\%). \quad (1)$$

The resultant precursor was loaded onto a Ni plate and placed at the center of an alumina tube reactor to prevent contamination from the reactor walls. After the reactor was purged with N_2 gas, the sample was heated at 673 K for 15 h under a flow of dry NH_3 (heating ramp: 10 K min^{-1}, flow rate: 100 mL min^{-1}) unless otherwise stated.

Synthesis of nano-TiO_2:N,F

Nano-TiO_2:N,F was synthesized under the optimized conditions reported previously.[14] Briefly, JRC-TIO-6 and $(NH_4)_2TiF_6$ were mixed in a molar ratio of 95 to 5 (*i.e.*, C = 5) in the presence of acetone using an agate mortar and pestle. The nitridation conditions were identical to those used for the preparation of meso-TiO_2:N,F.

Synthesis of bulk-TiO_2:N,F

Bulk-TiO_2:N,F was synthesized *via* a previously reported method.[16] Commercial rutile TiO_2 and $(NH_4)_2TiF_6$ were mixed in a molar ratio of 85 to 15 (*i.e.*, C = 15) in the presence of methanol using an agate mortar and pestle. The resultant precursor was loaded onto a Ni plate and placed at the center of an alumina tube reactor. After the reactor was purged with N_2 gas, the sample was heated at 773 K for 1 h under a dry NH_3 flow (ramp: 10 K min^{-1}, flow rate: 50 mL min^{-1}).

General characterization

X-ray diffraction (XRD) patterns were recorded on a MiniFlex600 (Rigaku) powder diffractometer. Raman spectra were acquired using a NRS-4500 spectrometer with a 532 nm laser (JASCO). UV-vis diffuse-reflectance spectra were obtained using a V-670 (JASCO) spectrometer equipped with an integration sphere. The specific surface area was calculated with the BELMaster software based on the Brunauer–Emmett–Teller (BET) theory. The surface morphology was observed by field-emission scanning electron microscopy (FE-SEM; S-5500; Hitachi High-Tech), and the amounts of N and F were determined using an

elemental analyzer (Elemental Analyzer-1; JM10, JM11; J-Science). Transmission electron microscopy (TEM) and reflection electron microscopy (REM) images were acquired using a field-emission transmission electron microscope (JEM-2100F; JEOL) and a scanning electron microscope (JCM-7000; JEOL), respectively. The cross section of the sample was prepared using a cross-section polisher (CP; SM-09010; JEOL) with an Ar-ion beam. Elemental analysis, SEM, TEM, REM, and CP were conducted at the Core Facility Center, Institute of Science Tokyo. Ti K-edge X-ray absorption fine structure (XAFS) measurements were performed at beamline 9A of the Photon Factory (High Energy Accelerator Research Organization, Tsukuba, Japan). Time-resolved microwave conductivity (TRMC) measurements were carried out for powdered samples prepared on adhesive tape on a quartz substrate. All of the experiments were conducted at room temperature in air. X-band microwave radiation with a frequency of ~9 GHz was used. The third harmonic (355 nm) of a Nd:YAG laser (Continuum, Surelite II, 5–8 ns pulse duration, 10 Hz) was used for carrier excitation (incident photon density $I_0 = 9.1 \times 10^{15}$ photons cm^{-2} $pulse^{-1}$). The photoconductivity ($\Delta\sigma = \Delta P_r/(AP_r)$, where A is the sensitivity coefficient, P_r is the reflected microwave power, and ΔP_r is the change in P_r during the irradiation) was converted into the product of the quantum yield (φ) and the sum of the charge carrier mobilities $\Sigma\mu$ ($= \mu^+ + \mu^-$) using the relational formula $\varphi\Sigma\mu = \Delta\sigma(eI_0F_{light})^{-1}$, where e and F_{light} are the electron charge and a correction coefficient, respectively.

Electrochemical impedance measurements

Meso-TiO_2 and meso-TiO_2:N,F (C = 15) electrodes were prepared *via* electrophoretic deposition onto conductive glass substrates coated with a fluorine-doped tin oxide (FTO) layer. Two FTO glasse plates were immersed in parallel (1.6 cm apart) into an acetone dispersion containing 50 mg of meso-TiO_2 or meso-TiO_2:N,F powder and 10 mg of I_2 in 45 mL of solution. A DC voltage of 30 V was applied for 15 s using a power supply (GW Instek PSW 80–13.5), resulting in uniform photocatalyst coatings on the FTO surfaces. The coated area was fixed at 1.5 cm × 3.5 cm. After deposition, the electrodes were dried under vacuum overnight.

Electrochemical impedance measurements were performed at room temperature using a potentiostat (HZ-Pro, Hokuto Denko) and a three-electrode electrochemical cell made of Pyrex glass. The working electrodes were meso-TiO_2/FTO and meso-TiO_2:N,F (C = 15)/FTO. An Ag/AgCl (saturated KCl) electrode and a Pt wire were used as the reference and counter electrodes, respectively. The electrolyte was an aqueous 0.1 M Na_2SO_4 solution whose pH was adjusted by the addition of H_2SO_4 or NaOH solution as needed. Prior to the start of the measurement, the solution was purged with Ar gas for 30 min to remove dissolved O_2. Mott–Schottky (MS) plots were recorded at a frequency of 100 Hz. Cyclic voltammetry (CV) was performed for 30 cycles over the potential range from −0.63 to +0.98 V (*vs.* reversible hydrogen electrode (RHE)).

Photocatalytic reactions

Photocatalytic reactions were conducted in a top-irradiation-type Pyrex reaction vessel connected to a closed gas circulation system.[30] In each experiment, 50 mg of meso-TiO_2:N,F and 200 mg of La_2O_3 (pre-calcined at 1273 K for 2 h to serve as a pH adjuster) were dispersed in 140 mL of a 10 mM $AgNO_3$ aqueous solution. The system was evacuated several times to remove air, and a small amount of Ar gas was introduced prior to irradiation. A 300 W Xe lamp was used as the light source (typically operated at 20 A), and illumination was conducted through a water filter and an L42 cutoff filter ($\lambda > 400$ nm) in combination with a CM-1 cold mirror. Evolved gases were analyzed using an on-line gas chromatograph (GC-8A, Shimadzu) equipped with a thermal conductivity detector and a molecular sieve 5A column; Ar was used as the carrier gas. During irradiation, the reaction temperature was maintained at room temperature by cooling water circulated around the reaction vessel.

The apparent quantum yield (AQY) for the water oxidation reaction was measured using the same experimental setup, and was calculated using eqn (2):

$$\text{AQY}\ (\%) = A \times R/I \times 100 \quad (2)$$

where A, R, and I represent a coefficient based on the reaction (A = 4 for O_2 evolution), the O_2 evolution rate, and the rate of incident photons, respectively.[31,32] The total number of incident photons (~0.40 mW) was measured using a calibrated Si photodiode.

Results and discussion

X-ray diffraction and elemental analyses

The as-prepared meso-TiO_2 was found to crystallize in a single rutile phase, and no phase transition was observed during the nitridation process at 673 K to yield the C = 0 sample, as confirmed by XRD analysis (Fig. 1(A)). With increasing concentration of $(NH_4)_2TiF_6$ (*i.e.*, increasing C value), impurities such as anatase TiO_2 and $TiOF_2$ appeared, particularly at high C values (C = 25 and 50), consistent with previous reports.[13,16] The absence of impurity phases at lower C values suggests that the impurities are caused by the direct pyrolysis of $(NH_4)_2TiF_6$ that had not reacted with meso-TiO_2.[33]

Raman spectroscopy

Raman spectroscopy was employed to investigate the local structure of the synthesized materials. The Raman spectrum of meso-TiO_2 exhibits a weak peak at 235 cm^{-1} (multi-photon process) and two intense peaks at 446 and 612 cm^{-1}, corresponding to the E_g- and A_{1g}-modes, respectively. These features are consistent with rutile-phase TiO_2 prepared by the hydrothermal method.[34–36] Peak broadening and slight frequency shifts became more pronounced with increasing C value, except for C = 50, which can be attributed to variations in particle size and/or slight non-stoichiometry induced by oxygen vacancies.[37] In particular, the E_g peak, sensitive to local inhomogeneity and lattice distortion around dopants, underwent a successive shift toward lower frequencies with increasing the C value, indicating strong influence of N doping into the rutile TiO_2 lattice.

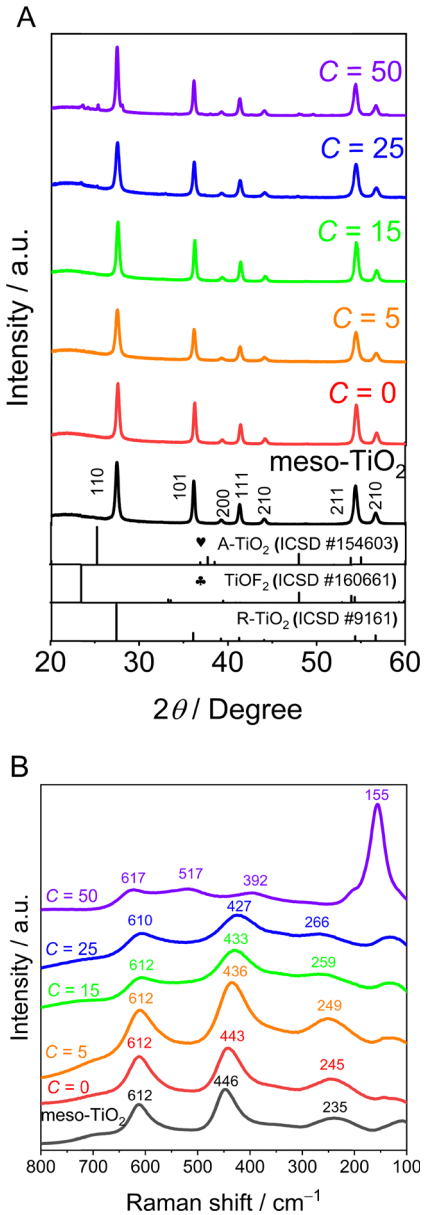

Fig. 1 (A) XRD patterns and (B) Raman spectra for meso-TiO_2 and meso-TiO_2:N,F obtained by nitriding mixtures of meso-TiO_2 and $(NH_4)_2TiF_6$ with different C values.

For C = 50, additional peaks at 155 and 517 cm^{-1} were observed, which are assigned to anatase TiO_2 and $TiOF_2$ impurities, respectively.[34,38] This observation is consistent with the XRD result (Fig. 1(B)).

Elemental analysis was conducted to confirm the presence of N and F in the doped meso-TiO_2 samples. Compared with the C = 0 sample, the samples with higher C values exhibited greater substitution of N^{3-} for O^{2-} in the TiO_2 lattice (for $C \geq 5$), indicating that F compensates for the charge imbalance caused by N doping and thus enables the incorporation of a greater amount of N (Table 1). As expected, the F content increased with the addition of more $(NH_4)_2TiF_6$. Interestingly, the N content showed a volcanic-type trend; increasing the

Table 1 Results of elemental analysis and N_2 adsorption/desorption measurements for meso-TiO_2:N,F prepared with different C values

Entry	C	Amount[a]/wt% N	Amount[a]/wt% F	Specific surface area[b]/m^2 g^{-1}	Total pore volume[c]/cm^3 g^{-1}
1[d]	—	—	—	43	0.061
2	0	0.50	—	21	0.13
3	5	0.52	1.3	18	0.065
4	15	0.81	2.0	14	0.042
5	25	1.1	3.2	10	0.035
6	50	0.96	5.5	4	0.011

[a] Determined by elemental analysis. [b] Determined by nitrogen adsorption/desorption measurements at liquid nitrogen temperature according to the BET method. [c] Determined by nitrogen adsorption/desorption measurements at $p/p^0 \sim 1$. [d] Precursor oxide.

C value from 25 to 50 led to a decrease in the N concentration. This observation suggests that excessive $(NH_4)_2TiF_6$ may lead to decomposition or structural disruption that hinders further N doping.

N_2 adsorption–desorption isotherms

N_2 adsorption–desorption experiments were performed for meso-TiO_2, meso-TiO_2:N (C = 0), and meso-TiO_2:N,F ($C \geq 5$) (Fig. 2). The isotherms for meso-TiO_2 exhibited a Type IV profile with an H3 hysteretic loop, in which the lower limit of the desorption branch corresponds to the cavitation-induced region.[39] This type of loop is typically observed in mesoporous materials composed of non-rigid aggregates of flaky particles, as will be discussed later. With increasing C values during the nitridation process, the H3-type hysteresis gradually disappeared, accompanied by a notable decrease in the specific area and the total pore volume (Table 1). These results indicate that a greater degree of nitridation, while beneficial for introducing N and F into the meso-TiO_2 lattice and thereby enhancing visible-light absorption, simultaneously leads to degradation of the mesoporous structure.

Electron microscopy

The microwave-assisted solvothermal method allowed for the formation of monodispersed TiO_2 particles, although some irregularly shaped particles were also observed (Fig. 3(A)). Some of the particles are spherical, with an average diameter of ~3 μm (Fig. 3(B)). They were composed of nanoparticles ranging from several tens of nanometers in size (Fig. 3(C)). The aggregation of these nanoparticles likely contributed to the observed porous structure, as supported by the N_2 adsorption–desorption isotherms (Fig. 2).

Precise control over the mesostructure and morphology in TiO_2 synthesis remains challenging because of the rapid hydrolysis and peptization of Ti precursors.[40] Although various synthetic strategies such as sol–gel, template-assisted, and hydrothermal methods have been developed, they often involve time-consuming procedures and harsh reaction conditions.[41–46] Moreover, mesoporous TiO_2 materials synthesized *via* self-assembly approaches typically consist of anatase nanocrystals because the formation of the rutile phase generally requires

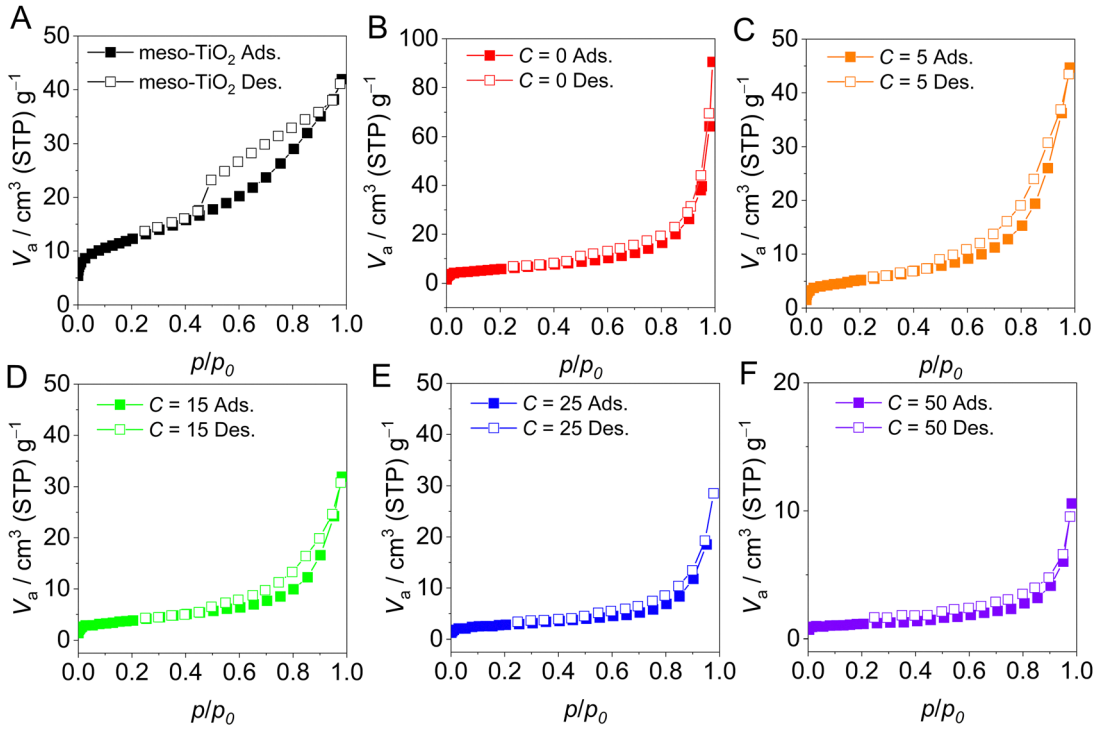

Fig. 2 N_2 adsorption–desorption isotherms of (A) as-prepared meso-TiO_2 and (B)–(F) meso-TiO_2:N,F with different *C* values.

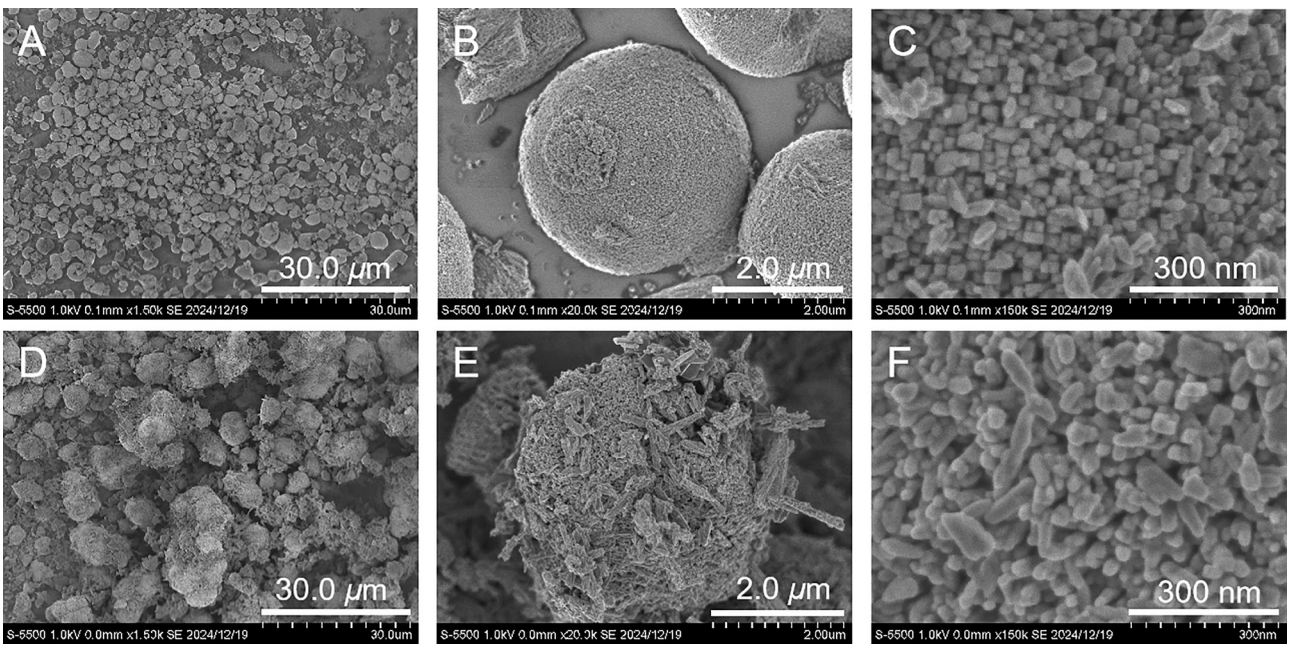

Fig. 3 SEM images of (A)–(C) as-prepared meso-TiO_2 and (D)–(F) meso-TiO_2:N,F with *C* = 15.

higher crystallization temperatures that can collapse the mesostructure as a result of thermal instability.[47]

In our microwave-assisted solvothermal method, the use of an organic solvent and HCl effectively moderated the hydrolysis of the Ti precursor, allowing a balance between rapid hydrolysis and controlled self-assembly while also suppressing excessive crystal growth. Microwave heating further reduced the temperature required for rutile phase formation and enabled the rapid construction of mesoporous TiO_2 microspheres with a well-defined rutile phase. This synthesis was achieved *via* micelle-assisted assembly in a sealed autoclave within a remarkably short reaction time.

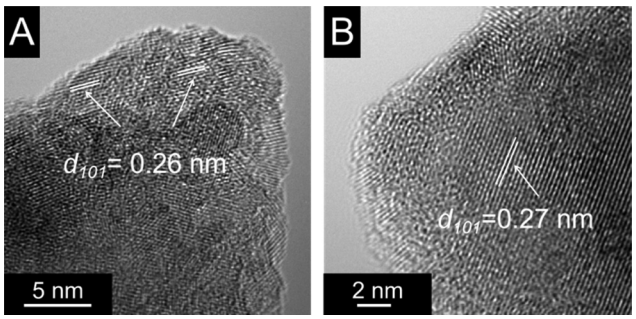

Fig. 4 TEM images of (A) the as-prepared meso-TiO_2 and (B) the C = 15 sample.

After the nitridation with $(NH_4)_2TiF_6$ (C = 15), the spherical morphology of meso-TiO_2 was largely retained, although some surface roughening and particle growth were observed (Fig. 3(D) and (E)). These changes are attributed to the growth of smaller primary particles upon N/F co-substitution (Fig. 3(F)), which also contributed to the reduced pore volume discussed in the previous section. The thermal ammonolysis of meso-TiO_2 with $(NH_4)_2TiF_6$ was accompanied by inevitable particle growth and the formation of anatase and $TiOF_2$ impurities, the latter becoming more prominent at higher initial concentrations of $(NH_4)_2TiF_6$.

TEM images of the meso-TiO_2 and the C = 15 sample (Fig. 4) revealed distinct lattice fringes with spacings of 0.26–0.27 nm, consistent with the (101) facet of rutile TiO_2. Given the similar ionic radii of N^{3-}, F^-, and O^{2-}, the preservation of the lattice spacing is reasonable. These results demonstrate successful topochemical conversion of meso-TiO_2 into TiO_2:N,F (here, C = 15) while retaining crystallinity, although partial degradation of the original mesoporous structure was observed.

Optical properties and bandgap structures

UV-vis diffuse-reflectance spectroscopy (DRS) measurements were performed on meso-TiO_2:N (C = 0) and meso-TiO_2:N,F ($C \geq 5$) samples to investigate their optical properties (Fig. 5). The spectra of both the meso-TiO_2:N (C = 0) and meso-TiO_2:N,F (C = 5) samples exhibited a new absorption band in the visible range (400–700 nm), in addition to the original absorption edge of meso-TiO_2 at ~400 nm. The N,F co-doped samples exhibited substantially stronger visible-light absorption than the N-doped sample, primarily because of enhanced N incorporation facilitated by F co-doping. The absorption extending beyond 600 nm is attributable to reduced Ti species, which may form under high-temperature ammonolysis with NH_3 gas acting as a reductant.[16,48]

As reported by Asahi *et al.*, N doping introduces N 2p orbitals above the O 2p valence band, effectively narrowing the bandgap.[49] F doping, by contrast, has been reported to primarily modify the electronic structure around the conduction-band edge of TiO_2.[50] Therefore, the co-substitution of N and F is expected to synergistically narrow the bandgap of meso-TiO_2, enhancing its visible-light absorption.

Because rutile TiO_2 is considered an indirect-bandgap semiconductor, we estimated the bandgaps of meso-TiO_2 and

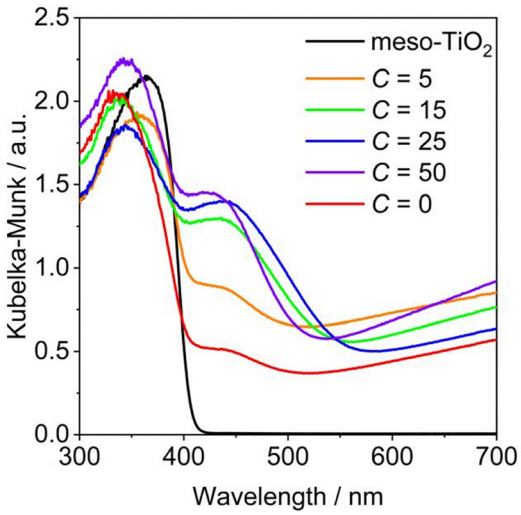

Fig. 5 UV-vis diffuse-reflectance spectra of as-prepared meso-TiO_2 and meso-TiO_2:N,F with different C values.

meso-TiO_2:N,F (C = 15) from Tauc plots using the square root of the Kubelka–Munk function (Fig. S1).[30,51,52] The bandgap decreased substantially from 3.03 eV (meso-TiO_2) to 2.25 eV (C = 15), consistent with the green coloration of the doped sample (Fig. S2).

The electrochemical properties were further examined by CV and MS analyses. The C = 15 sample displayed stable redox behavior under both anodic and cathodic polarization across multiple CV cycles (Fig. S3), indicating good electrochemical stability. The band edge potential could be estimated from electrochemical impedance measurements. MS plots showed a positive slope, confirming the n-type semiconductor character of the as-prepared materials (Fig. S4). The flat-band potentials were estimated to be −0.86 V and −0.62 V *vs.* Ag/AgCl at pH 6.4 for meso-TiO_2 and the C = 15 sample, respectively.

On the basis of previous reports,[16,53] we assumed a 0.2 V difference between the conduction-band potential and the flat-band potential. Under this assumption, in conjunction with the bandgaps and the flat-band potentials estimated from DRS and MS plots, we can depict the bandgap structure (Fig. S5). The conduction-band potential for TiO_2:N,F is approximately the same as that for undoped rutile TiO_2.[16] In the present study, we confirmed this trend for the C = 15 sample, supporting the validity of this assumption.

X-ray absorption spectroscopy

The effect of co-substitution of N and F into rutile TiO_2 on the electronic state of Ti was also confirmed by Ti-K edge X-ray absorption near edge structure (XANES) spectra. The pre-edge structure at the Ti-K edge for TiO_2 features three peaks: A1, A2, and A3 (Fig. 6(A)). The A_1 peak is assigned to the quadrupole transition from 1s to t_{2g} of the local Ti absorber. The A_2 peak originates from the overlap of two transitions, which are the quadrupole transition from 1s to e_g of the local Ti absorber and the dipole transition from 1s to t_{2g} of neighboring Ti atoms. The A_3 peak is attributed to the dipole transition from 1s to e_g

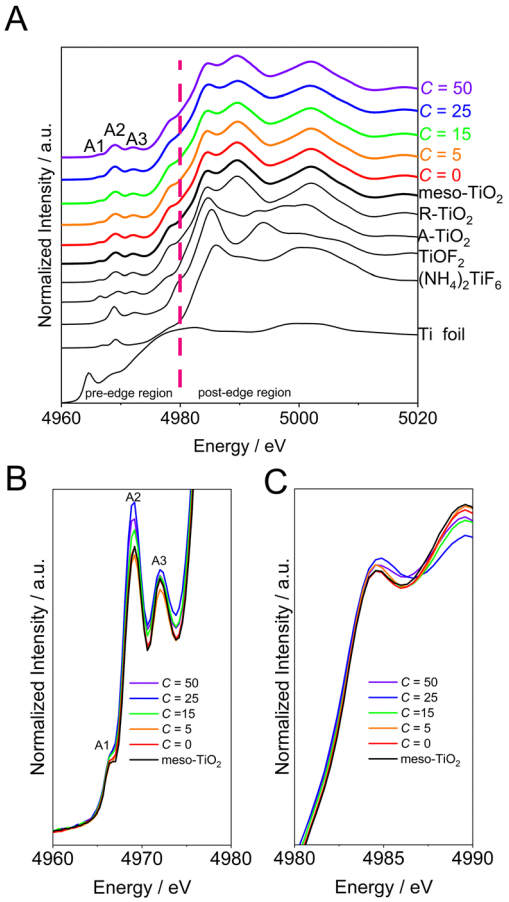

Fig. 6 Ti K-edge XANES spectra of as-prepared meso-TiO_2 and meso-TiO_2:N,F with different C values. (A) Entire XANES spectrum and (B) pre-edge and (C) white-line regions.

of the neighboring Ti atoms.[54,55] The XANES spectra of the meso-TiO_2:N,F samples resemble that of rutile TiO_2. However, the relative intensity of A2 increased with increasing C value (Fig. 6(B)), indicating increased distortion of the octahedral TiO_6 unit.[56] In addition, the post-edge features also provide information on the local structure of Ti. The main peak in the post-edge region resembles that for rutile TiO_2; however, the edge crest of the white line peak at ~4984 eV is substantially broadened with increasing C value, indicating the loss of long- and medium-range order (Fig. 6(C)).[57]

Photogenerated charge carrier dynamics

The photogenerated charge carrier dynamics of the as-prepared meso-TiO_2:N,F samples were evaluated by time-resolved microwave conductivity (TRMC) measurements. TRMC is a powerful technique for probing the dynamic behavior of charge carriers in semiconductor materials, with numerous examples being reported in mixed-anion compounds.[58–61] Although the literature includes TRMC studies for TiO_2,[62–64] no such studies have yet been reported for TiO_2:N,F.

Fig. 7 shows the time-dependent TRMC signals for meso-TiO_2 and meso-TiO_2:N,F samples with different C values. The corresponding values of $\varphi\Sigma\mu_{max}$ and $\tau_{1/2}$ are summarized in

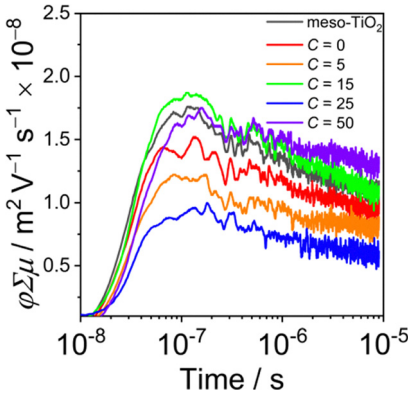

Fig. 7 TRMC transient decay profiles of as-prepared meso-TiO_2 and meso-TiO_2:N,F samples with different C values.

Table S1. In general, aliovalent substitution of an element into a host material causes a charge imbalance, which promotes charge carrier recombination.[12,65] The reduced $\varphi\Sigma\mu_{max}$ (*i.e.*, photoconductivity) for the C = 0 sample compared with that for pristine meso-TiO_2 is attributed to the detrimental effects of N^{3-}/O^{2-} substitution on carrier mobility. Interestingly, this attenuation in photoconductivity was not observed in the C = 15 sample, suggesting that an optimal level of N/F co-doping does not exacerbate charge recombination. Instead, it may enhance carrier transport dynamics relative to those in the undoped meso-TiO_2. However, increasing the C value to 25 led to a noticeable decrease in photoconductivity, likely due to the introduction of additional recombination centers associated with excessive doping. The TRMC profile for the C = 50 sample appears more complex, which is attributable to the higher concentration of impurity phases, including anatase TiO_2 (or TiO_2:N,F) and $TiOF_2$ (Fig. 1).

Photocatalytic water oxidation

A volcano-like trend was observed between the O_2 generation rate and the C value (Fig. 8(A)), with the highest photocatalytic activity being obtained at C = 15, which gave an AQY of 5.2% at 365 nm. The time course of O_2 evolution over the optimal meso-TiO_2:N,F composition is shown in Fig. 8(B). The full time-course data for

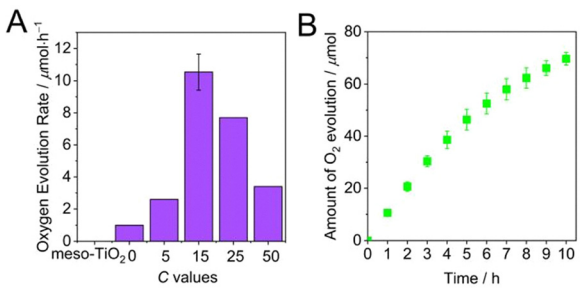

Fig. 8 Photocatalytic activity of meso-TiO_2:N,F with different C values for O_2 evolution under visible-light irradiation in $AgNO_3$ aqueous solution. Reaction conditions: photocatalyst, 50 mg; La_2O_3, 200 mg; 10 mM $AgNO_3$ aqueous solution, 140 mL; light source, 300 W Xe lamp fitted with a CM-1 mirror and an L42 cutoff filter (λ > 400 nm).

the other specimens are compared with those for $C = 15$ in Fig. S6. As the reaction proceeds, the reaction rate gradually decreases from 10.6 μmol h^{-1} during the first hour to 3.6 μmol h^{-1} after 10 h. This decrease is attributed to the reduction of Ag^+ ions in the solution to metallic Ag on the surface of the photocatalyst; the metallic Ag not only occupies the active sites but also interferes with light absorption, ultimately leading to a decrease in the reaction rate.[66] The optimized meso-TiO_2:N,F exhibited greater activity than previously reported nano-TiO_2:N,F and bulk-TiO_2:N,F (Fig. S7).

Factors influencing the photocatalytic activity

The results of the photocatalytic reactions indicated that the photocatalytic activity of meso-TiO_2:N,F was strongly dependent on the C value in the synthesis and that the highest activity was obtained with the $C = 15$ sample. Here, morphology (or porosity), visible-light absorption capability, and photoconductivity are factors considered to affect the photocatalytic activity of meso-TiO_2:N,F. A porous structure may be beneficial for charge carrier migration from the bulk to the surface and for mass transport of reactants. Materials with more pronounced visible-light absorption can, in principle, generate more photogenerated charge carriers, which may participate in surface chemical reactions, depending on the photoconductivity of the material.

Meso-TiO_2 did not show activity under visible light because it did not exhibit visible-light absorption (Fig. 5). The $C = 0$ and 5 samples exhibited more pronounced visible-light absorption than meso-TiO_2 because of the N/F incorporation. Therefore, meso-TiO_2 doped with N or co-doped with N/F at $C = 0$ or 5 showed photocatalytic activity under visible-light irradiation, although the photoconductivity was lower than that of meso-TiO_2 (Fig. 7 and 8). The decrease in photoconductivity is not favorable for improving photocatalytic activity. Nevertheless, the fact that the $C = 0$ and 5 samples showed photocatalytic activity under visible-light irradiation strongly suggests that the visible-light absorption capacity is a major factor influencing the photocatalytic activity. However, the visible-light absorption of the $C = 0$ and 5 samples is not sufficient because of their lower N content (Table 1 and Fig. 5), which may lead to lower photocatalytic activity than for the $C = 15$ sample, although the mesoporous structure could be maintained.

Although the $C = 25$ sample had the highest N content among the synthesized meso-TiO_2:N,F samples and a morphological character similar to that for the $C = 15$ sample, its O_2 evolution rate was lower than that for the $C = 15$ sample. One possible explanation for the decrease in activity is that the excess N/F doping increased the density of electron–hole recombination centers.[48] This idea is consistent with the TRMC measurement results, which indicated that the photoconductivity was attenuated from $C = 15$ to $C = 25$ (Fig. 7). A correlation between photocatalytic O_2 evolution rate and photoconductivity has been reported previously. For example, the photocatalytic O_2 evolution rate over the oxyhalides Bi_4TaO_8Cl and $PbBiO_2Cl$ has been reported to be correlated with the product of the maximum TRMC signal ($\varphi\Sigma\mu_{max}$) and the half-lifetime of charge carriers ($\tau_{1/2}$).[59,60]

For rutile TiO_2, the rate of O_2 evolution from aqueous $AgNO_3$ tends to increase with increasing particle size of rutile TiO_2 (*i.e.*, with increasing crystallinity of rutile TiO_2).[67,68] The higher activity of the bulk TiO_2:N,F compared with that of the nano-TiO_2:N,F (Fig. S7) is subject to this trend, although the weaker visible-light absorption of nano-TiO_2:N,F may contribute to the lower activity to a certain extent (Fig. S8). Interestingly, the meso-TiO_2:N,F exhibited even higher activity than the bulk TiO_2:N,F. Although the specific surface areas of the meso-TiO_2:N,F and the bulk-TiO_2:N,F are similar, their morphological characteristics differ.[16] This observation again suggests that the mesoporous structure may contribute to the higher activity of the TiO_2:N,F.

Meanwhile, a comparison of the photoconductivity and half-lifetime of the $C = 15$ sample with those of bulk-TiO_2:N,F is intriguing. The photoconductivity ($\varphi\Sigma\mu_{max}$) of the $C = 15$ sample was lower than that of bulk TiO_2:N,F, whereas its half-lifetime was much longer. As a result, the product of $\varphi\Sigma\mu_{max}$ and $\tau_{1/2}$ for the $C = 15$ sample was greater than that for bulk-TiO_2:N,F, which may be another explanation for the higher activity of the $C = 15$ sample. Notably, N and F co-substitution led to a pronounced attenuation of the TRMC signals in both nano- and bulk-TiO_2, whereas an enhancement was observed exclusively in the meso-TiO_2 (Fig. S9). This result suggests that co-doping of N and F introduces additional defects into the nano and bulk forms, thereby hindering the transport of photogenerated carriers. By contrast, the unique structure of the mesoporous TiO_2 presumably promotes efficient transport of photogenerated charge carriers within the nanochannels, leading to improved charge carrier mobility.

The importance of retaining a mesoporous structure was further underscored using another set of meso-TiO_2:N,F samples synthesized with a fixed C value of 15 but subjected to different ammonolysis temperatures. Thermal ammonolysis at 623 K failed to yield single-phase rutile TiO_2:N,F, and temperatures above 673 K were required to achieve phase purity (Fig. S10). However, N_2 adsorption–desorption measurements revealed that such a high-temperature treatment led to collapse of the mesoporous structure (Fig. S11), despite the concomitant enhancement in visible-light absorption (Fig. S12). Consequently, the sample that simultaneously retained the mesoporous texture derived from the meso-TiO_2 precursor and exhibited no impurity phases showed the highest photocatalytic activity (Fig. S13). These results clearly demonstrate that maximizing the O_2 evolution activity in rutile TiO_2:N,F requires a delicate balance between enhancing visible-light absorption and preserving the mesoporous architecture.

Conclusions

We successfully synthesized mesoporous rutile TiO_2:N,F photocatalysts *via* a topotactic ammonolysis approach using mesoporous rutile-type TiO_2 (meso-TiO_2) as a precursor. Notably, the synthesis of rutile-type meso-TiO_2 without a template—previously considered difficult—was achieved under mild

conditions (low temperature and short reaction time) with the aid of microwaves, representing a significant advance in inorganic synthesis.[69,70] Co-substitution of N and F into the rutile lattice modulated the electronic structure of Ti and extended visible-light absorption while simultaneously inducing local distortion of the TiO_6 octahedra. Systematic studies revealed that the visible-light-driven O_2 evolution activity was governed by a delicate balance between doping-induced light absorption and retention of the mesoporous framework. Although high-temperature ammonolysis enhanced visible-light absorption by promoting N incorporation, it also disrupted the mesostructure, resulting in decreased photocatalytic performance. The best-performing sample was obtained under conditions that allowed for both phase-pure rutile formation and preservation of the mesoporous texture, enabling efficient separation of photogenerated charge carriers. These findings underscore the critical importance of structural control in designing non-metal-doped oxide photocatalysts for solar energy conversion. While the optimized meso-TiO_2:N,F does not yet match the activity of state-of-the-art photocatalysts such as $BiVO_4$, further improvement is expected through the introduction of suitable O_2 evolution cocatalysts. Moreover, the high surface area of TiO_2-based mesostructures suggests broader potential as adsorbents or catalyst supports for capturing harmful gases such as NO_x and volatile organic compounds.[71,72] Ongoing work in our group is directed toward these applications.

Author contributions

S. L. and K. M. designed the project and wrote a draft of the manuscript. S. L. conducted most of the experiments and analyses with X. Z. R. N., F. I. and A. S. performed the time-resolved microwave conductivity measurements. M. O. provided comments on experiments. All of the authors made contributions to the preparation of the manuscript.

Conflicts of interest

There are no conflicts to declare.

Data availability

The data supporting this article have been included as part of the supplementary information (SI). Supplementary information: additional characterization and reaction data. See DOI: **https://doi.org/10.1039/d5nh00584a**.

Acknowledgements

This work was supported by Grant-in-Aid for Scientific Research (A) (JP25H00899). It was also partially supported by Grant-in-Aids for Transformative Research Areas (A) ''Supra-ceramics'' (JP22H05142, JP22H05148 and JP 23H04626).

Notes and references

1 S. Sun, Y.-C. Zhang, G. Shen, Y. Wang, X. Liu, Z. Duan, L. Pan, X. Zhang and J.-J. Zou, *Appl. Catal., B*, 2019, **243**, 253–261.
2 Z. Wang, C. Li and K. Domen, *Chem. Soc. Rev.*, 2019, **48**, 2109–2125.
3 J. Xing, W. Q. Fang, H. J. Zhao and H. G. Yang, *Chem. – Asian J.*, 2012, **7**, 642–657.
4 J. Yan, J. Liu, Y. Ji, M. Batmunkh, D. Li, X. Liu, X. Cao, Y. Li, S. Liu and T. Ma, *ACS Catal.*, 2020, **10**, 8742–8750.
5 G. Ge, M. Liu, C. Liu, W. Zhou, D. Wang, L. Liu and J. Ye, *J. Mater. Chem. A*, 2019, **7**, 9222–9229.
6 P. Li, L. Kong, J. Liu, J. Yan and S. Liu, *ACS Sustainable Chem. Eng.*, 2019, **7**, 17941–17949.
7 M. M. S. Karim, A. M. Ganose, L. Pieters, W. W. W. Leung, J. Wade, L. Zhang, D. O. Scanlon and R. G. Palgrave, *Chem. Mater.*, 2019, **31**, 9430–9444.
8 Q. Wang, M. Nakabayashi, T. Hisatomi, S. Sun, S. Akiyama, Z. Wang, Z. Pan, X. Xiao, T. Watanabe, T. Yamada, N. Shibata, T. Takata and K. Domen, *Nat. Mater.*, 2019, **18**, 827–832.
9 H. Fujito, H. Kunioku, D. Kato, H. Suzuki, M. Higashi, H. Kageyama and R. Abe, *J. Am. Chem. Soc.*, 2016, **138**, 2082–2085.
10 S. Wei and X. Xu, *Appl. Catal., B*, 2018, **228**, 10–18.
11 M. Hojamberdiev, R. Vargas, Z. C. Kadirova, K. Kato, H. Sena, A. G. Krasnov, A. Yamakata, K. Teshima and M. Lerch, *ACS Catal.*, 2022, **12**, 1403–1414.
12 A. Nakada, S. Nishioka, J. J. M. Vequizo, K. Muraoka, T. Kanazawa, A. Yamakata, S. Nozawa, H. Kumagai, S.-I. Adachi, O. Ishitani and K. Maeda, *J. Mater. Chem. A*, 2017, **5**, 11710–11719.
13 K. Nukumizu, J. Nunoshige, T. Takata, J. N. Kondo, M. Hara, H. Kobayashi and K. Domen, *Chem. Lett.*, 2003, **32**, 196–197.
14 A. Miyoshi, K. Kato, T. Yokoi, J. J. Wiesfeld, K. Nakajima, A. Yamakara and K. Maeda, *J. Mater. Chem. A*, 2020, **8**, 11996–12002.
15 H. A. Seibel Ii, P. Karen, T. R. Wagner and P. M. Woodward, *J. Mater. Chem.*, 2009, **19**, 471–477.
16 A. Miyoshi, J. J. M. Vequizo, S. Nishioka, Y. Kato, M. Yamamoto, S. Yamashita, T. Yokoi, A. Iwase, S. Nozawa, A. Yamakata, T. Yoshida, K. Kimoto, A. Kudo and K. Maeda, *Sustainable Energy Fuels*, 2018, **2**, 2025–2035.
17 Y. Takahara, J. N. Kondo, T. Takata, D. Lu and K. Domen, *Chem. Mater.*, 2001, **13**, 1194–1199.
18 X. Wang, K. Maeda, X. Chen, K. Takanabe, K. Domen, Y. Hou, X. Fu and M. Antonietti, *J. Am. Chem. Soc.*, 2009, **131**, 1680–1681.
19 J. B. Joo, I. Lee, M. Dahl, G. D. Moon, F. Zaera and Y. Yin, *Adv. Funct. Mater.*, 2013, **23**, 4246–4254.
20 D. S. Kim, S. J. Han and S. Y. Kwak, *J. Colloid Interface Sci.*, 2007, **316**, 85–91.
21 T. Wang, X. Meng, P. Li, S. Ouyang, K. Chang, G. Liu, Z. Mei and J. Ye, *Nano Energy*, 2014, **9**, 50–60.
22 D. M. Antonelli and J. Y. Ying, *Angew. Chem., Int. Ed.*, 2003, **34**, 2014–2017.

23 W. Li, Z. Wu, J. Wang, A. A. Elzatahry and D. Zhao, *Chem. Mater.*, 2013, **26**, 287–298.
24 J. H. Pan, X. S. Zhao and W. I. Lee, *Chem. Eng. J.*, 2011, **170**, 363–380.
25 Y. Zhang, G. Li, Y. Wu, Y. Luo and L. Zhang, *J. Phys. Chem. B*, 2005, **109**, 5478–5481.
26 Y. Kobayashi, O. J. Hernandez, T. Sakaguchi, T. Yajima, T. Roisnel, Y. Tsujimoto, M. Morita, Y. Noda, Y. Mogami, A. Kitada, M. Ohkura, S. Hosokawa, Z. Li, K. Hayashi, Y. Kusano, J. Kim, N. Tsuji, A. Fujiwara, Y. Matsushita, K. Yoshimura, K. Takegoshi, M. Inoue, M. Takano and H. Kageyama, *Nat. Mater.*, 2012, **11**, 507–511.
27 F. D. Romero, A. Leach, J. S. Moller, F. Foronda, S. J. Blundell and M. A. Hayward, *Angew. Chem., Int. Ed.*, 2014, **53**, 7556–7559.
28 T. Oshima, T. Ichibha, K. Oqmhula, K. Hibino, H. Mogi, S. Yamashita, K. Fujii, Y. Miseki, K. Hongo, D. Lu, R. Maezono, K. Sayama, M. Yashima, K. Kimoto, H. Kato, M. Kakihana, H. Kageyama and K. Maeda, *Angew. Chem., Int. Ed.*, 2020, **59**, 9736–9743.
29 Y. Tang, K. Kato, T. Oshima, H. Mogi, A. Miyoshi, K. Fujii, K. I. Yanagisawa, K. Kimoto, A. Yamakata, M. Yashima and K. Maeda, *Inorg. Chem.*, 2020, **59**, 11122–11128.
30 S. Nishioka, F. E. Osterloh, X. Wang, T. E. Mallouk and K. Maeda, *Nat. Rev. Methods Primers*, 2023, **3**, 42.
31 K. Maeda, T. Maeda, C. Suppaso, S. Nishioka, Y. Kamakura, S. Yasuda and T. Yokoi, *Sustainable Energy Fuels*, 2024, **8**, 36–42.
32 C. Wang, H. Zhang, W. Luo, T. Sun and Y. Xu, *Angew. Chem., Int. Ed.*, 2021, **60**, 25381–25390.
33 D. Chen, Z. Jiang, J. Geng, J. Zhu and D. Yang, *J. Nanopart. Res.*, 2008, **11**, 303–313.
34 J. Yang, S. Mei, J. M. Ferreira, P. Norby and S. Quaresma, *J. Colloid Interface Sci.*, 2005, **283**, 102–106.
35 C. T. Cherian, M. V. Reddy, T. Magdaleno, C.-H. Sow, K. V. Ramanujachary, G. V. S. Rao and B. V. R. Chowdari, *CrystEngComm*, 2012, **14**, 978–986.
36 H. L. Ma, J. Y. Yang, Y. Dai, Y. B. Zhang, B. Lu and G. H. Ma, *Appl. Surf. Sci.*, 2007, **253**, 7497–7500.
37 Y. Huo, Y. Jin, J. Zhu and H. Li, *Appl. Catal., B*, 2009, **89**, 543–550.
38 S. Guan, Q. Fan, Z. Shen, Y. Zhao, Y. Sun and Z. Shi, *J. Mater. Chem. A*, 2021, **9**, 5720–5729.
39 M. S. Mel'gunov, *Adsorption*, 2022, **29**, 199–208.
40 W. Zhou and H. Fu, *ChemCatChem*, 2013, **5**, 885–894.
41 R. O. Da Silva, R. H. Goncalves, D. G. Stroppa, A. J. Ramirez and E. R. Leite, *Nanoscale*, 2011, **3**, 1910–1916.
42 P. A. R. Bleta and L. Lorenzato, *J. Phys. Chem. C*, 2010, **114**, 2039–2048.
43 J. B. Joo, Q. Zhang, I. Lee, M. Dahl, F. Zaera and Y. Yin, *Adv. Funct. Mater.*, 2011, **22**, 166–174.
44 D. V. Bavykin, V. N. Parmon, A. A. Lapkin and F. C. Walsh, *J. Mater. Chem.*, 2004, **14**, 2581–2587.
45 J. Yu, G. Wang, B. Cheng and M. Zhou, *Appl. Catal., B*, 2007, **69**, 171–180.
46 Z. Wang, D. Li, X. Zhang, H. Yu, K. Deng, Y. Xu, H. Wang and L. Wang, *ACS Appl. Nano Mater.*, 2024, **7**, 9868–9873.
47 K. Lan, R. Wang, W. Zhang, Z. Zhao, A. Elzatahry, X. Zhang, Y. Liu, D. Al-Dhayan, Y. Xia and D. Zhao, *Chem*, 2018, **4**, 2436–2450.
48 Y. W. Irie and K. Hashimoto, *J. Phys. Chem. B*, 2003, **107**, 5483–5486.
49 T. M. Asahi, T. Ohwaki, K. Aoki and Y. Taga, *Science*, 2001, **293**, 269–271.
50 T. Yamaki, T. Umebayashi, T. Sumita, S. Yamamoto, M. Maekawa, A. Kawasuso and H. Itoh, *Nucl. Instrum. Methods Phys. Res., Sect. B*, 2003, **206**, 254–258.
51 Y. Wu, M. Xing, B. Tian, J. Zhang and F. Chen, *Chem. Eng. J.*, 2010, **162**, 710–717.
52 S. Suzuki, A. Iwase and A. Kudo, *Catal. Sci. Technol.*, 2020, **10**, 4912–4916.
53 Y. Matsumoto, *J. Solid State Chem.*, 1996, **126**, 227–234.
54 L. X. Chen, T. Rajh, Z. Wang and M. C. Thurnauer, *J. Phys. Chem. B*, 1997, **101**, 10688–10697.
55 T. Uozumi, A. Kotani and J. C. Parlebas, *J. Electron Spectrosc. Relat. Phenom.*, 2004, **137–140**, 623–627.
56 S. Nozawa, T. Iwazumi, H. Osawa and T. Uozumi, *Appl. Phys. Express*, 2013, **6**, 061501.
57 D. R. M. Schwartz, D. R. Mullins, W. Yan, H. Zhu, S. Dai and S. H. Overbury, *J. Phys. Chem. C*, 2007, **111**, 17322–17332.
58 K. Aihara, R. Mizuochi, M. Okazaki, S. Nishioka, S. Yasuda, T. Yokoi, F. Ishiwari, A. Saeki, M. Inada and K. Maeda, *ACS Mater. Lett.*, 2023, **5**, 2355–2360.
59 H. Suzuki, M. Higashi, H. Kunioku, R. Abe and A. Saeki, *ACS Energy Lett.*, 2019, **4**, 1572–1578.
60 H. Suzuki, S. Kanno, M. Hada, R. Abe and A. Saeki, *Chem. Mater.*, 2020, **32**, 4166–4173.
61 H. Tsuchikado, S. Anabuki, O. Cretu, Y. Kinoshita, M. Hattori, Y. Shiroma, D. Fan, M. Okazaki, T. Soma, F. Ishiwari, S. Nozawa, T. Yokoi, M. Hara, K. Kimoto, A. Yamakata, A. Saeki and K. Maeda, *ACS Appl. Energy Mater.*, 2025, **8**, 3541–3552.
62 H. H. Scot, T. Martin, W. Choi and M. R. Hoffmann, *J. Chem. Soc., Faraday Trans.*, 1994, **90**, 3315–3322.
63 S. Nakajima and R. Katoh, *J. Mater. Chem. A*, 2015, **3**, 15466–15472.
64 A. Saeki, Y. Yasutani, H. Oga and S. Seki, *J. Phys. Chem. C*, 2014, **118**, 22561–22572.
65 K. D. Tsuyoshi and T. Takata, *J. Phys. Chem. C*, 2009, **113**, 19386–19388.
66 T. Hisatomi, C. Katayama, Y. Moriya, T. Minegishi, M. Katayama, H. Nishiyama, T. Yamada and K. Domen, *Energy Environ. Sci.*, 2013, **6**, 3595–3599.
67 H. Kominami, S.-Y. Murakami, J.-I. Kato, Y. Kera and B. Ohtani, *J. Phys. Chem. B*, 2002, **106**, 10501–10507.
68 O.-O. Prieto-Mahaney, N. Murakami, R. Abe and B. Ohtani, *Chem. Lett.*, 2009, **38**, 238–239.
69 J. Li, R. Li, W. Wang, K. Lan and D. Zhao, *Adv. Mater.*, 2024, **36**, e2311460.
70 A. Wang, Y. Ma and D. Zhao, *ACS Nano*, 2024, **18**, 22829–22854.
71 H. Ma, Y. Li, C. Wang, Y. Li and X. Zhang, *Catalysts*, 2025, **15**, 103.
72 S. Bagheri, N. Muhd Julkapli and S. Bee Abd Hamid, *Sci. World J.*, 2014, **2014**, 727496.